Available online at www.sciencedirect.com
SCIENCE DIRECT®
Journal of Crystal Growth 280 (2005) 320–334
JOURNAL OF CRYSTAL GROWTH
www.elsevier.com/locate/jcrysgro

Three-dimensional phase-field simulations of the effect of convection on free dendritic growth

Y. Lu, C. Beckermann*, J.C. Ramirez

Department of Mechanical and Industrial Engineering, The University of Iowa, Iowa City, IA 52242, USA

Received 21 January 2005; accepted 22 March 2005
Available online 4 May 2005
Communicated by G.B. McFadden

Abstract

Three-dimensional free dendritic growth of a pure material into an undercooled melt in the presence of fluid flow is investigated numerically using the phase-field method. Such computations are made possible by solving the Navier–Stokes equations for the flow and the energy equation for the heat transport on a grid that is twice as coarse as the grid for the phase-field equation. The effect of the flow on the upstream growing dendrite tip velocity and radius of curvature is investigated as a function of the imposed flow velocity, undercooling, crystalline anisotropy, and Prandtl number. The results are compared to available theories of dendritic growth with and without convection. The predicted growth Péclet numbers as a function of the flow Péclet number are in reasonable agreement with the theoretical predictions. The dendrite tip selection parameter is essentially independent of the flow velocity within the range studied, which is also in accordance with theory. The three-dimensional dendrite tip shape is found to be well fitted by the same universal scaling relation as without flow.

PACS: 68.70.+w; 81.30.Fb; 47.27.Te

Keywords: A1. Convection; A1. Crystal morphology; A1. Dendrites; A1. Growth models; A1. Solidification

1. Introduction

Dendritic solidification of crystalline materials is a complex pattern formation process that is governed by the combined action of heat transport (for pure materials) and surface tension. Understanding dendritic growth is important, for example, for predicting microstructures in solidified metals. In the absence of melt flow, a theory is available to predict the steady-state velocity, V, and radius of curvature, R_p, of the tip of a dendritic needle crystal of a pure substance

*Corresponding author. Tel.: +1 319 335 5681; fax: +1 319 335 5669.
E-mail address: becker@engineering.uiowa.edu (C. Beckermann).

0022-0248/$ - see front matter © 2005 Published by Elsevier B.V.
doi:10.1016/j.jcrysgro.2005.03.063

growing into an infinite volume of undercooled melt. The theory assumes that the dendrite is isothermal and that the interface shape is a paraboloid of revolution; the subscript p is used to indicate this parabolic shape assumption. The solution of the heat diffusion problem in the melt is given by

$$\Delta = \mathrm{Iv}(Pe_\mathrm{p}), \tag{1}$$

where Iv is the Ivantsov function [1], $\Delta = (T_\mathrm{m} - T_\infty)/(L/c_\mathrm{p})$ is the dimensionless melt undercooling, and $Pe_\mathrm{p} = R_\mathrm{p}V/(2D)$ is the tip growth Péclet number. Here, T_m and T_∞ are the equilibrium melting and far-field temperatures, L is the latent heat of fusion, c_p is the specific heat, and D is the thermal diffusivity. According to microscopic solvability theory [2,3], a unique tip velocity is then selected by the action of anisotropic surface tension via the scaling relation

$$\sigma_\mathrm{p}^* = 2Dd_0/(R_\mathrm{p}^2 V), \tag{2}$$

where d_0 is the capillary length. At low undercoolings, the selection parameter σ_p^* is a constant that only depends on the anisotropy strength ε_4 (for a crystal with cubic symmetry) as $\sigma_\mathrm{p}^* \sim \varepsilon_4^{7/4}$ in the limit of small anisotropy. The anisotropy also alters the parabolic tip shape according to [4]

$$x = \frac{r^2}{2} - A_4 r^4 \cos(4\varphi), \tag{3}$$

where (r, φ) are the polar coordinates in the plane normal to the growth direction ($-x$ direction) and all lengths are scaled by the tip radius R_p. The constant A_4 ($= \frac{1}{96} = 0.0104$ [5]) is independent of the anisotropy strength, implying that Eq. (3) represents a universal dendrite tip shape. The above theoretical predictions have recently been verified by numerical calculations using the phase-field method [6,7] and through comparisons with benchmark experiments [8–10]. Karma et al. [7] found A_4 to be in the range 0.004–0.005.

Convection in the melt has long been realized to have a profound effect on dendritic growth [11,12]. It is presently unclear how the above theory for dendritic growth under purely diffusive conditions should be modified to account for the convection effect. In particular, the selection of the operating state of the dendrite tip in the presence of melt flow has been the subject of some controversy, as reviewed below. Initial theoretical efforts have concentrated on deriving extensions to the Ivantsov solution for the case of undercooled melt flowing uniformly over a parabolic needle crystal from infinity in a direction opposite to the growth direction. Dash and Gill [13] derived an analytical expression that relates the undercooling Δ to the growth Péclet number, Pe_p, flow Péclet number, $Pe_\mathrm{f} = R_\mathrm{p}U/(2D)$, and Prandtl number, $Pr = \nu/D$, where U is the imposed far-field velocity and ν is the kinematic viscosity of the melt. They found that the heat flux from a dendrite tip modeled as a paraboloid of revolution is much larger than from a two-dimensional dendrite modeled as a parabolic cylinder, especially at small values of the flow Péclet number. Ananth and Gill [14–16], Saville and Beaghton [17], Ben Amar et al. [18], and Xu [19] obtained various analytical solutions for the effect of convection on the heat transport from parabolic dendrites (both parabolic cylinders and axisymmetric paraboloids) under Oseen viscous flow, potential flow, or other approximations. In the absence of flow, these solutions all reduce to Eq. (1). Through numerical studies, Lee et al. [20] determined that the Stokes flow approximation becomes inaccurate at large flow Péclet numbers and that flow influences the heat transport (in succinonitrile) significantly when the flow velocity is greater than the tip growth velocity. The only study found in the literature that extends solvability theory to include convection is by Bouissou and Pelce [21]. They assumed a parabolic cylinder tip shape and a uniform axial flow in two dimensions to derive an analytical expression for the variation of the tip selection parameter, σ_p^*, with flow velocity, U. In the large flow velocity limit, when $(d_0 U)/(R_\mathrm{p}V) = Pe_\mathrm{f}\sigma_\mathrm{p}^*$ is of the order of unity or greater, the theory predicts that the selection parameter decreases with U. At lower flow velocities σ_p^* is predicted to be independent of U. A more rigorous theory of dendritic growth with flow has remained lacking.

Experimental investigations of the operating state of a dendrite tip in the presence of a forced flow have failed to yield consistent results. Bouissou et al. [22] found that the selection parameter decreases for pivalic acid (PVA) den-

drites almost linearly with the longitudinal component of the external flow velocity, but is independent of the transverse component of the flow velocity. Emsellem and Tabeling [23] performed growth experiments using ammonium bromide and found σ_p^* to be almost independent of U in their experimental range. On the other hand, the experiments on succinonitrile (SCN) by Lee et al. [24] and Ananth and Gill [25] indicated that σ_p^* increases, rather than decreases, with increasing flow velocity.

In recent years, phase-field models have been extended to include melt convection [26–29], providing a unique means of studying the interactions between flow and solidification through numerical simulations. Using such phase-field models, several investigators have simulated the effect of convection on dendritic growth in two dimensions [30–35]. The same problem has also been simulated using other numerical techniques [36–39]. In particular, the phase-field simulation results of Tong et al. [30,33] showed good agreement with the two-dimensional (parabolic cylinder) Oseen–Ivantsov solution of Saville and Beaghton [17] for heat transport from a dendrite tip in the presence of an axial flow. Tong et al. found that the selection parameter σ_p^* does not depend on the flow velocity within the ranges of the parameters they varied, which is in agreement with the two-dimensional solvability theory of Bouissou and Pelce [21]. They were not able to verify the analytical expression of Ref. [21] for the large flow velocities where σ_p^* is predicted to decrease with U.

Three-dimensional phase-field simulations of the effects of convection on dendritic growth of a single crystal in an undercooled melt were performed by Jeong et al. [40,41] and Lu et al. [42]. Jeong et al. [40] found that the effect of flow on the upstream growing dendrite tip in two dimensions is much larger than in three dimensions. For the one three-dimensional simulation with flow they reported, the selection parameter σ_p^* for the upstream tip was lower than without flow. Jeong et al. [41] reported results of several three-dimensional simulations and compared them to the experiments of Bouissou et al. [22] and Lee et al. [24]. The results at high undercooling and high anisotropy agreed well with the transport solution for an axisymmetric paraboloid of Saville and Beaghton [17]. Some disagreement was observed at low undercooling where the flow field is modified by the presence of other dendrite branches. The selection parameter σ_p^* was found to decrease slightly with flow velocity, but the variations were small enough to be within the uncertainty of the calculations. All cases simulated were in a regime where the solvability theory of Bouissou and Pelce [21] predicts that σ_p^* is independent of U. Jeong et al. [41] conclude that significant open questions remain about the evolution of the dendritic microstructure when flow is present. Very recently, Al-Rawahi and Tryggvason [43] presented three-dimensional simulations of dendritic solidification with convection using a numerical technique that is based on explicit tracking of connected marker points to describe the solid–liquid interface, instead of the phase-field method. Although no quantitative comparisons were performed, the results showed the same trends as in Jeong et al. [40,41].

The present study uses three-dimensional phase-field simulations to investigate free dendritic growth of a pure substance in a forced flow. While parts of the study were already presented at conferences [42], this paper provides a more complete account of the method and includes several new results. The effects of flow on both the dendrite tip operating state and the tip shape are investigated and comparisons are made with available theories.

2. Phase-field model

The present model uses as a starting point the phase-field equation presented by Karma and Rappel [6] for three-dimensional dendritic growth of a pure substance in the presence of purely diffusive heat transport. In addition, the results of the thin-interface asymptotic analysis of Karma and Rappel [44] are exploited to render the computations more efficient and to investigate the limit of vanishing interface kinetics (i.e. local equilibrium at the solid–liquid interface). Convection is incorporated into the phase-field model

using the methodology developed by Beckermann et al. [27] and used by several other groups [30,33–35,40,41]. In this method, the phase-field equation is unchanged from the purely diffusive case, thus assuming that the phase-field is not advected by the flow and that the phase-transition temperature does not depend on pressure. These assumptions are appropriate for the purpose of the present study. The mass, momentum, and energy conservation equations are derived using an averaging technique that renders the equations valid everywhere in the domain, including the diffuse interface region. The usual no-slip condition at a sharp solid–liquid interface is enforced through a varying interfacial force term in the liquid momentum equation in the diffuse interface region. The force term is chosen such that the no-slip condition is accurately reproduced regardless of the diffuse interface width.

Let ψ denote the phase field, where $\psi = \pm 1$ refers to the bulk solid and liquid phases, respectively. The phase field varies smoothly from 1 in the solid to -1 in the liquid in a small but numerically resolvable diffuse interface region, and the solid–liquid interface is defined by the contour $\psi = 0$. The anisotropic form of the phase-field equation is given by [6]

$$\tau(\boldsymbol{n})\frac{\partial \psi}{\partial t} = [\psi - \lambda u(1-\psi^2)](1-\psi^2) + \nabla\cdot[W(\boldsymbol{n})^2\nabla\psi] + \sum_{\xi=x,y,z}\partial_\xi\left[|\nabla\psi|^2 W(\boldsymbol{n})\frac{\partial W(\boldsymbol{n})}{\partial(\partial_\xi\psi)}\right], \tag{4}$$

where λ is a dimensionless parameter that controls the coupling between the phase field and the temperature field, $\boldsymbol{n}$ is the interface normal vector, t is time, x, y, z are Cartesian coordinates, and $u = (T - T_m)/(L/c_p)$ is the dimensionless temperature. The interface width parameter W and the relaxation time τ depend on the orientation of the interface and are given by $W(\boldsymbol{n}) = W_0 a_s(\boldsymbol{n})$ and $\tau(\boldsymbol{n}) = \tau_0 a_s(\boldsymbol{n})^2$, respectively, with

$$a_s(\boldsymbol{n}) = (1-3\varepsilon_4)\times\left[1 + \frac{4\varepsilon_4}{1-3\varepsilon_4}\frac{(\partial_x\psi)^4 + (\partial_y\psi)^4 + (\partial_z\psi)^4}{|\nabla\psi|^4}\right]. \tag{5}$$

An effective anisotropy strength ε_e that provides a small correction to ε_4 due to the discreetness of the computational lattice can be calculated from [6]

$$\varepsilon_e = \varepsilon_4 - \frac{1}{240}\Delta x^2 + O(\varepsilon_4\Delta x^2) + O(\Delta x^4), \tag{6}$$

where Δx is the lattice spacing. Finally, from the thin-interface asymptotic analysis [44], and in the limit of vanishing interface kinetics, the phase-field parameters W_0, τ_0, and λ are related by

$$\frac{W_0}{d_0} = \frac{\lambda}{0.8839}, \tag{7}$$

$$\tau_0 = 0.6267\frac{\lambda W_0^2}{D}. \tag{8}$$

With these relations, the phase-field model converges to the sharp-interface model in the limit of a "thin" interface whose width is small compared to the scale of the microstructural pattern but larger than the capillary length. Convergence studies are carried out by decreasing the dimensionless interface width W_0/d_0 until results are independent of W_0/d_0. For this purpose, the governing equations are non-dimensionalized using W_0 and W_0^2/D as length and time scales, respectively. This way, the thermal diffusivity is eliminated from the equations and only λ is left as a free parameter. Simulation results for different values of the interface width W_0/d_0, are obtained by changing λ according to Eq. (7). This procedure is slightly different from previous convergence studies [33] where the governing equations are non-dimensionalized using W_0 and τ_0 as length and time scales, respectively. This choice of scales introduces a dimensionless thermal diffusivity $D\tau_0/W_0^2$ which, according to Eq. (8), is linearly proportional to λ. To obtain results for different values of W_0/d_0, both λ and $D\tau_0/W_0^2$ have to be varied according to Eqs. (7) and (8).

Let ϕ denote a solid fraction that is related to the phase field by $\phi = (\psi + 1)/2$, and hence varies from 0 in the liquid to 1 in the solid. The governing mass, momentum, and energy conservation equa-

tions of the present phase-field model, assuming constant properties and equal densities and thermal diffusivities of the solid and liquid phases, are given, respectively, by [27]

$$\nabla \cdot [(1-\phi)\boldsymbol{V}] = 0, \tag{9}$$

$$\begin{aligned}\partial[(1-\phi)\boldsymbol{V}]/\partial t + (1-\phi)\boldsymbol{V}\cdot\nabla\boldsymbol{V} \\ = -(1-\phi)\nabla p/\rho + \nu\nabla^2[(1-\phi)\boldsymbol{V}] \\ - 2\nu h\phi^2(1-\phi)\boldsymbol{V}/W_0^2,\end{aligned} \tag{10}$$

$$\partial u/\partial t + (1-\phi)\boldsymbol{V}\cdot\nabla u = D\nabla^2 u + \partial\phi/\partial t, \tag{11}$$

where $\boldsymbol{V}$ is the liquid velocity vector, p is the pressure, and ρ is the density. The last term on the right-hand side of Eq. (10) is a distributed interfacial term that forces the velocity to vanish as $\phi \to 1$; the constant h is equal to 2.757 as determined from an asymptotic analysis for a simple shear flow past a diffuse interface [27]. As mentioned earlier, the important property of this term is that the velocity profile smoothly approaches the profile for a sharp interface with a no-slip condition at $\phi = 0.5$ (or $\psi = 0$), regardless of the diffuse interface width. The last term on the right-hand side of Eq. (11) is a volumetric latent heat release term.

3. Computational procedures and problem description

The phase-field equation, Eq. (4), is solved using the same explicit finite difference code and uniform grid as Karma and Rappel [6] and the reader is referred to that reference for all details of the numerical implementation. The energy equation, Eq. (11), is also discretized using an explicit finite difference method, but with a grid spacing Δx that is exactly twice as large as the one for the phase-field equation, as already described in Ref. [42]. The temperatures are linearly interpolated to the phase field nodes for the solution of the phase-field equation. The intent of this double-grid method is to reduce computational time and memory requirements without sacrificing accuracy. It is made possible by the fact that the temperature gradients inside the diffuse interface are much smaller than the ones associated with the hyperbolic tangent profile of the phase field. The double-grid method gives essentially identical results as using a single grid spacing [42].

The mass and momentum conservation equations, Eqs. (9) and (10), are solved using a modified version of the implicit finite element code FEATFLOW [45,46]. This code uses a multi-grid solver and error control methods that make it both robust and efficient. The modifications relate primarily to the presence of the terms in Eqs. (9) and (10) that contain the solid fraction ϕ. The same (coarse) node spacing is employed for the flow equations as for the energy equation [42]. The present double-grid scheme reduces the computational time by up to 80%, because most of the time is spent solving for the flow field. Equally important, the memory requirements are vastly reduced. Using a coarser grid for the flow field is made possible in large part by the excellent convergence properties, with respect to the diffuse interface width, of the interfacial force term in Eq. (10). The flow algorithm has been validated against numerous benchmark problems [47]. Further reductions in the computational time can be obtained by using the dual time-step algorithm introduced in Refs. [30,33] and also used in Refs. [40,41]. In that scheme, the flow equations are solved using a time step that is up to ten times larger than the one for the phase-field and energy equations. However, this procedure was not utilized in the present study because it does not result in a reduction in the computer memory requirement. All computations were performed on PCs that have a memory of 2 GB and took typically several days to complete.

Only one example of a validation study performed to test the flow algorithm and code is presented here. The example is concerned with steady flow around an infinite cylinder at low Reynolds numbers [47]. The rectangular domain and numerical mesh employed are shown in Fig. 1. The dimensions of the domain are 10, 10, and 0.8 (in dimensionless length units) in the x, y, and z directions, respectively. Fluid enters the domain at

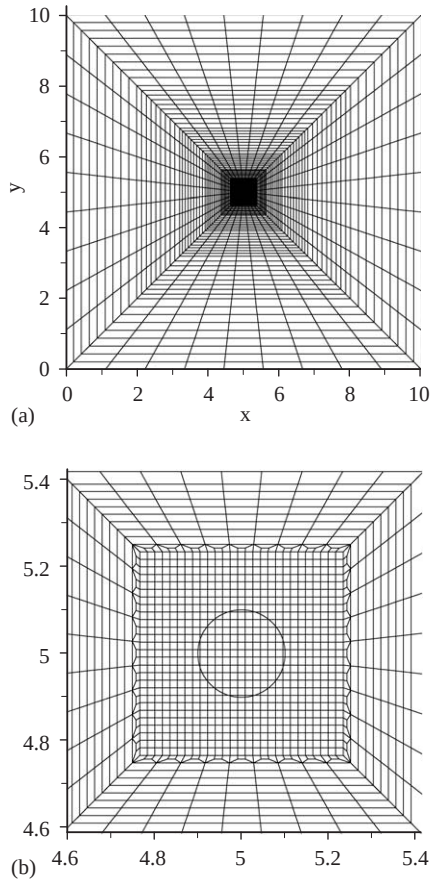

Fig. 1. Two-dimensional x–y cut of the non-uniform mesh used for solving the benchmark problem of low Reynolds number flow around a circular cylinder; the cylinder axis is in the z-direction, and the mesh in the z-direction is a simple extension of the cut shown above; the domain size is $10 \times 10 \times 0.8$: (a) complete view of the mesh in the x–y plane; (b) enlarged view of the mesh in the center region of the domain. The cylinder is defined by a (stationary) distribution of the phase-field variable, with a hyperbolic tangent variation across the cylinder–fluid interface (circle).

the $x = 0$ plane with a uniform inlet velocity and leaves at $x = 10$ with zero longitudinal velocity gradients. Slip (zero stress) boundary conditions are applied at the other four boundary planes. The cylinder axis at the center of the x–y plane extends over the entire z direction of the domain. Together with the slip boundary conditions at $z = 0$ and 0.8, the flow in the z direction is uniform and the length of the cylinder in the simulation does not matter.

In order for the flow field not to be affected by the domain boundaries, the cylinder diameter is taken as 0.2, which is 50 times smaller than the height or length of the domain. The number of nodal points is kept relatively small by using a non-uniform mesh in the x–y plane, as shown in Fig. 1. The cylinder is defined by a stationary distribution of the phase field variable, such that $\psi = 1$ inside the cylinder, $\psi = -1$ in the bulk fluid, and $\psi = -\tanh(n/(\sqrt{2}W_0))$ across the diffuse interface, which corresponds to the stationary solution of the phase-field equation. The $\psi = 0$ contour is shown in Fig. 1b. The interface width parameter is chosen equal to $W_0 = \Delta x/1.6$, where Δx is the (uniform) mesh spacing at the center of the domain where the cylinder is located (see Fig. 1b). This choice is the same as in the following dendrite simulations and implies that 96% of the variation in ψ is contained within $4\Delta x$. Note from Fig. 1b that the entire cylinder diameter is only about $12\Delta x$. Such a coarse mesh is chosen on purpose in order to assess the accuracy of the double-grid scheme for the smallest dendrite feature encountered in the following. Using the computed flow results, the drag coefficient, C_D, of the cylinder was determined as a function of the Reynolds number. Fig. 2 shows a comparison of the predicted drag coefficients with previous

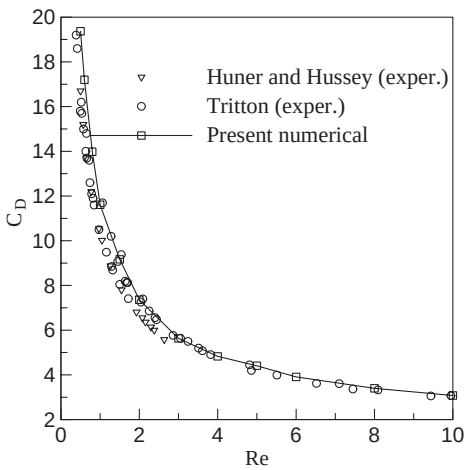

Fig. 2. Comparison of measured and predicted drag coefficients as a function of Reynolds number for flow across an infinitely long circular cylinder.

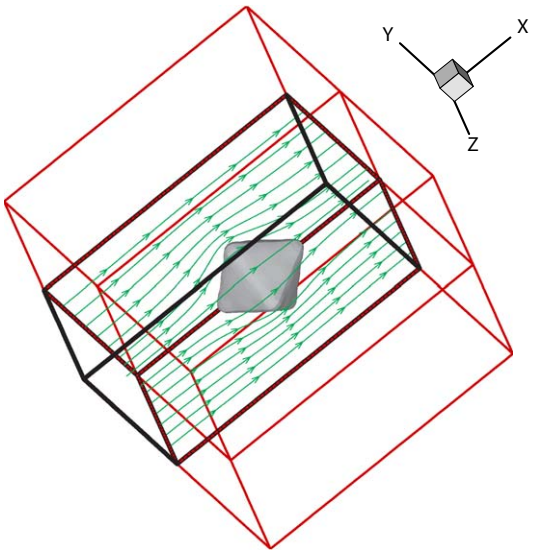

Fig. 3. Schematic of the computational domain; the size of the outer box (thin lines) is $(204.8W_0)^3$; due to symmetry, computations are performed in a quarter of the box only (heavy lines).

experimental measurements [48,49]. Excellent agreement can be observed over the entire Reynolds number range.

The physical system used in the dendritic growth simulations is shown in Fig. 3. The entire domain is a cube with a side length of $204.8W_0$ and a crystal seed located at its center. However, computations are only performed in the quarter of the domain that is outlined by the thick solid lines in Fig. 3. This symmetry assumption is appropriate for the small flow Reynolds numbers considered here. The melt enters the domain at the $x = 0$ plane with a uniform velocity U and undercooling Δ, and leaves the domain at $x = 204.8W_0$ with zero gradients in the x-direction. On the four planes normal to the inlet and outlet, slip boundary conditions are imposed for the velocity and symmetry conditions for the phase field and temperature. The crystalline directions of the seed are aligned with the coordinate axes. To save computational time, the seed is allowed to grow for some time before the flow is imposed. All dendrite growth calculations with flow reported in the following are performed using a uniform mesh spacing of $\Delta x = 0.8W_0$ ($256 \times 128 \times 128$ finite-difference nodes) for the phase-field equation and $\Delta x = 1.6W_0$ for the other equations, according to the double-grid scheme. For the finite element mesh, this corresponds to 545,025 vertices, 1,593,344 nodes, and 524,288 elements. With this mesh, the domain is large enough that, for the ranges of the governing parameters investigated in the present study, the upstream growing dendrite tip can reach a steady state without the thermal and velocity boundary layers in front of it interfering with the domain boundary. However, other parts of the dendrite (see Fig. 4), in particular the tips growing normal to and downstream of the flow, do not reach a steady growth regime, as shown below.

Two different methods are used to characterize the shape of the dendrite tip growing upstream in the $-x$ direction. The actual tip radius is denoted by R and represents the local radius of curvature of the solid–liquid interface at the very dendrite tip. It is calculated from the phase-field contours in the x–y ($\varphi = 0^\circ$) plane using the method detailed in Appendix B in Karma and Rappel [6].

The "parabolic" tip radius, R_p, on the other hand, represents the tip radius of a paraboloid of revolution that is fitted to the actual nonaxisymmetric phase-field shape away from the tip using the "equal cross-sectional area" (ECSA) method described in Section III.A in Karma et al. [7]. In this method, the cross-sectional area of solid normal to the growth direction is calculated from $S(x) = \int \phi(x, y, z)\,dy\,dz$. A plot of $S(x)$ away from the tip can be fitted to a straight line and the parabolic tip radius is then given by the slope of this line according to $R_p = S(x)/[2\pi(x_0 - x)]$ for $x < x_0$, where x_0 is the position of the tip. Karma et al. [7] showed that in the absence of flow, R_p coincides (to within numerical accuracy) with the tip radius that is obtained from the Ivantsov relation, Eq. (1), using the tip velocity from the phase-field dendrite. They also confirmed that this agreement is independent of undercooling and anisotropy strength. In the absence of flow R_p is therefore a good scaling parameter for the entire dendrite shape. The question of whether this is still true in the presence of flow will be addressed below.

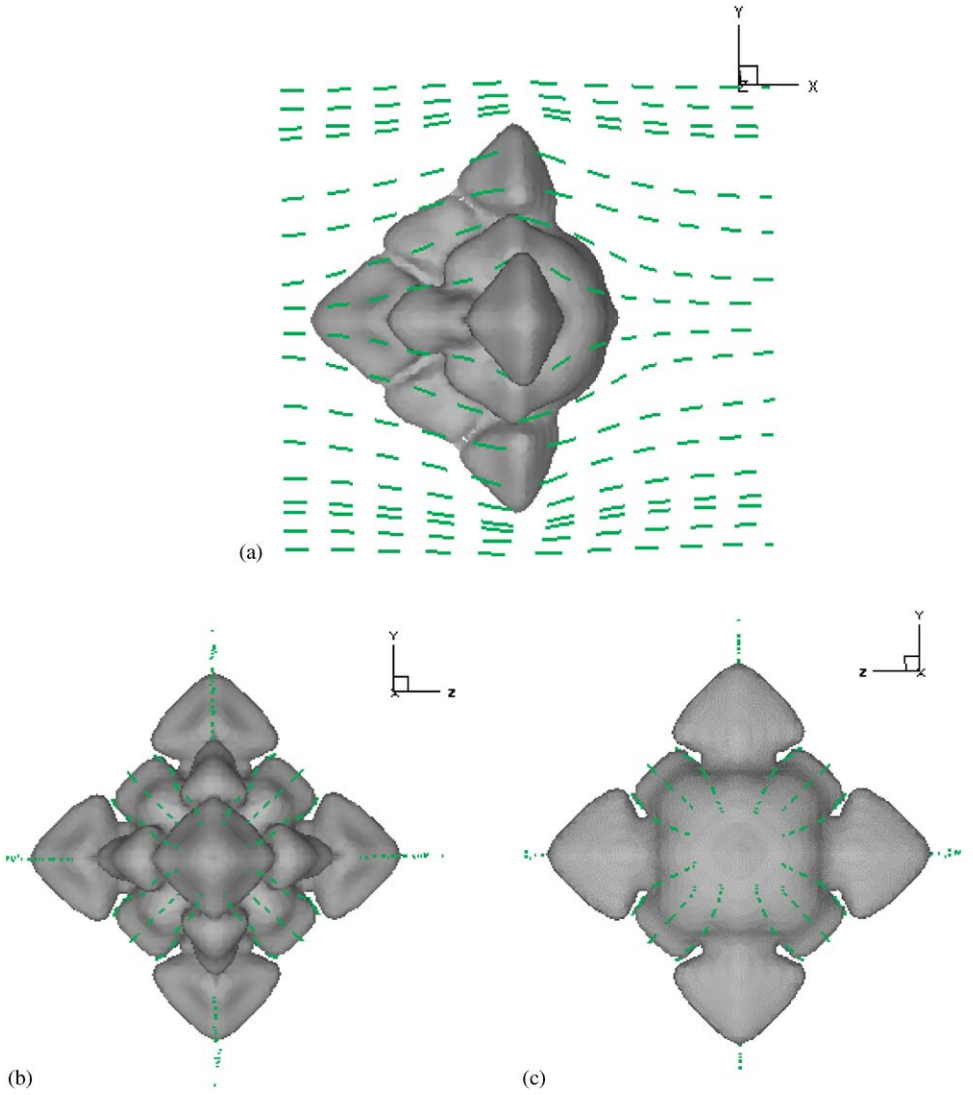

Fig. 4. Example of a computed dendrite morphology with flow ($\Delta = 0.55$, $U\tau_0/W_0 = 1$, $\varepsilon_4 = 0.05$, $Pr = 2.5$, $D\tau_0/W_0^2 = 4$, and $\lambda = 6.383$): (a) side view (flow is from left to right); (b) downstream view; (c) upstream view.

4. Simulation results and comparisons with theory

4.1. Growth morphology in the presence of convection

Fig. 4 shows different views of a typical dendrite simulated in the presence of flow. The simulation parameters are: $\Delta = 0.55$, $U\tau_0/W_0 = 1$, $\varepsilon_4 = 0.05$, $Pr = 2.5$, $D\tau_0/W_0^2 = 4$, and $\lambda = 6.383$. It can be seen that convection has a strong effect on the growth morphology when comparing it to a completely symmetric dendrite that would be obtained under purely diffusive conditions. The upstream facing tips and branches grow at a much faster rate than the downstream oriented parts of the dendrite, because the temperature gradients on the upstream side are larger due to the impinging flow. The four "fins" of the upstream growing dendrite arm that reflect the underlying cubic anisotropy can be seen in Fig. 4b. The melt is

heated by the dendrite as it flows around it, which causes the downstream parts to grow more slowly than even in the purely diffusive case. Fig. 4c shows that the development of the downstream arm is almost completely suppressed. The tips of the four dendrite arms oriented normal to the flow direction grow at approximately the same rate as in the purely diffusive case. Even though the normal dendrite arms are much thicker on the upstream side (Fig. 4a), their growth axis (approximated by a straight line extending from the center of the seed to the tip of the arm) is not deflected by more than $1-2^{\circ}$ in the upstream direction.

Figs. 5a and b show the calculated variation of the dendrite tip velocities, Vd_0/D, and radii, R/d_0, respectively, as a function of time, tD/d_0^2, for the following set of parameters: $\Delta = 0.45$, $\varepsilon_4 = 0.04$, $Pr = 3.85$, and $\lambda = 3$. Results are shown for a simulation without flow and for a simulation with $UW_0/D = 1$, where the flow was started at $tD/d_0^2 = 16$. It can be seen that the no-flow dendrite reaches a steady growth regime at about $tD/d_0^2 = 50$, after which the tip velocity and radius attain constant values. In the case with flow, the upstream tip reaches a steady growth regime already at about $tD/d_0^2 = 40$. For this simulation, the upstream steady tip velocity is about 53% higher than in the no-flow case, while the radius is about 9% lower. The tip velocity of the cross-stream dendrite arm reaches a steady-state value that is very close to the no-flow result, but due to its slight deflection it was not possible to evaluate its tip radius using the method of Ref. [6]. The downstream dendrite tip does not reach a steady growth regime and continues to slow down (with the tip radius increasing). This can be explained by the continually increasing size of the dendrite upstream of it. In the following subsections, only the steady state results for the upstream growing dendrite tip are considered further.

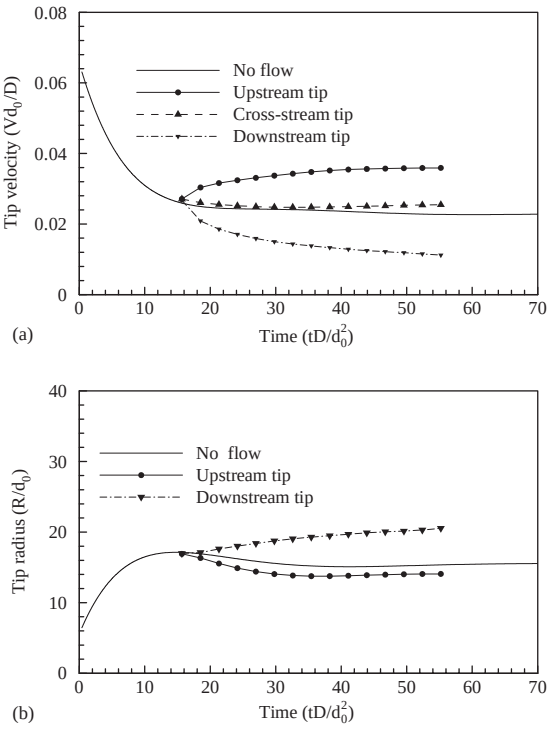

Fig. 5. Temporal evolution of: (a) tip velocity; (b) tip radius ($\Delta = 0.45$, $UW_0/D = 1$, $\varepsilon_4 = 0.04$, $Pr = 3.85$, and $\lambda = 3$).

4.2. Comparison with Jeong et al. [40,50]

Table 1 shows a comparison of various upstream dendrite tip growth parameters with results of Jeong et al. [40,50] for a simulation typical of the cases considered in the present study. The actual tip radius, R, is used in the calculation of the growth Péclet number, Pe, and the selection parameter, σ^*. Overall, good agreement is obtained with the results of Jeong et al. [40,50] for both the no-flow and the flow cases. The small differences can be attributed to uncertainties in the

Table 1
Comparison of calculated upstream dendrite tip growth parameters with Jeong et al. [40,50]

$\varepsilon_4 = 0.05$, $\Delta = 0.55$, $Pr = 23.1$, $D\tau_0/W_0^2 = 4$, $\lambda = 6.383$, $d_0/W_0 = 0.139$

	No flow		$U\tau_0/W_0 = 1$	
	Jeong et al.	Present	Jeong et al.	Present
Vd_0/D	0.0317	0.0307	0.0359	0.0337
R/d_0	20.9	21.6	25.3	26.9
Pe	0.332	0.332	0.454	0.452
σ^*	0.144	0.139	0.0872	0.0820

evaluation of the tip velocity and radius [40] and in deciding when the tip has reached a complete steady growth state. Note that the comparison in Table 1 is for a dimensionless interface width parameter of $W_0/d_0 = 7.2$ (or $\lambda = 6.383$), which is the value used in Jeong et al. [40]. The following dendrite simulations are all performed for an interface width that is smaller by more than a factor of two (i.e. $W_0/d_0 = 3.4$ or $\lambda = 3$), which results in better convergence with respect to the interface width [see discussion below Eq. (8)]. The convergence studies presented in Refs. [6,7,33,47] show that with $\lambda = 3$ (and $\Delta x/W_0 = 0.625$), accurate results, that are reasonably independent of the interface width, are obtained for the dendrite tip velocity and radius for the same range of undercoolings and anisotropy strengths as investigated here.

4.3. Péclet number comparison

Ananth and Gill [14] and Saville and Beaghton [17] provide analytical solutions for the heat transport from a steadily growing, isothermal, and axisymmetric parabolic dendrite tip for the case of undercooled melt flowing uniformly over the tip from infinity in a direction opposite to the growth direction. The solutions are complex relations of the form

$$\Delta = f(Pe_p = R_p V/(2D), \quad Pe_f = R_p U/(2D), Pr = \nu/D) \tag{12}$$

which reduce to the Ivantsov solution, Eq. (1), in the limit of now flow, i.e. $Pe_f = 0$. While both solutions [14,17] are based on the Oseen viscous flow (small Reynolds number) approximation, they are of a somewhat different form, presumably because they are derived using different analytical techniques. In order to compare the present three-dimensional numerical results for the upstream growing dendrite tip with the above analytical solutions for a paraboloid of revolution, the "equal cross-sectional area" (ECSA) method [7], described in Section 3, is used to determine the parabolic tip radius, R_p, from the computed phase-field contours.

Fig. 6 shows a comparison of steady-state growth Péclet numbers extracted from the simulations for the upstream growing dendrite tip with the Oseen–Ivantsov relations, Eq. (12) [14,17], as a function of the flow Péclet number. The flow Péclet number is varied by performing several simulations with different imposed melt velocities, U. The imposed melt undercooling and the Prandtl number are fixed at $\Delta = 0.45$ and $Pr = 3.85$, respectively. Two sets of phase-field simulations are performed for anisotropy strengths of $\varepsilon_4 = 0.04$ (circles) and 0.05 (squares). For the open symbols in Fig. 6, the actual dendrite tip radius, R, is used to evaluate both the growth and the flow Péclet numbers, while the parabolic tip radius, R_p, is used for the filled symbols. As expected, the phase-field results and the theories show that the growth Péclet number increases with increasing flow velocity. As observed previously for the two-dimensional case [6,33], the Péclet numbers based on the actual tip radius are in poor agreement with the theories, which can be attributed to the computed dendrite shape deviating significantly

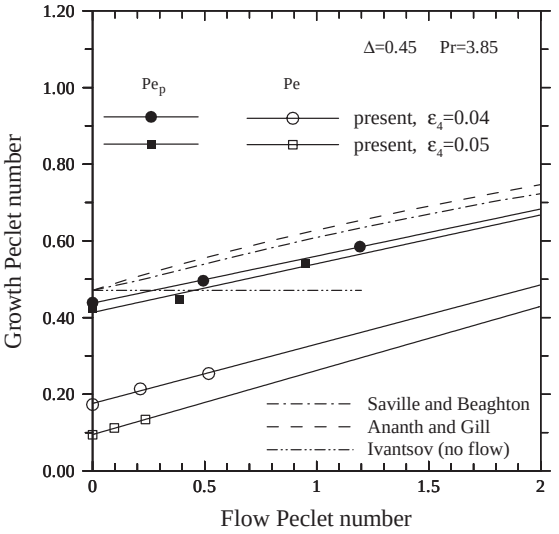

Fig. 6. Comparison of predicted growth Péclet numbers as a function of the flow Péclet number with Oseen–Ivantsov theories [14,17] for $\Delta = 0.45$, $Pr = 3.85$, $\lambda = 3$, and $\varepsilon_4 = 0.04$ and 0.05; for the open symbols, the actual dendrite tip radius, R, is used to evaluate both the growth and the flow Péclet numbers, while the parabolic tip radius, R_p, is used for the filled symbols.

from a paraboloid. In fact, the growth Péclet numbers based on the actual tip radius from the simulations for the two anisotropy strengths (0.04 and 0.05) differ by almost a factor of two, illustrating the strong effect of the anisotropy strength on the dendrite shape close to the tip. On the other hand, the growth Péclet numbers based on the parabolic tip radius, Pe_p, are in much better agreement with the Oseen–Ivantsov theories. Due to the fitting of the computed dendrite shape to a paraboloid of revolution, the computed Pe_p for the two anisotropy strengths fall along almost the same line. Note that the two theoretical results [14,17], do not differ significantly from each other.

In Fig. 6, the Pe_p from the phase-field simulations fall consistently below the curves from the Oseen–Ivantsov theories by up to about 10%. This is somewhat surprising, since Karma et al. [7] showed for the three-dimensional case that in the absence of flow, the computed Pe_p coincides to within a numerical accuracy of about 1% with the Péclet number that is obtained from the Ivantsov relation, Eq. (1), for a given undercooling. This excellent agreement is remarkable, since the computed dendrite is neither axisymmetric nor isothermal. The present disparity can be explained by an insufficient fitting range used for determining the parabolic tip radius from the computed dendrite shape (Section 3). Fig. 7 shows the ratio R_p/R_{Iv} as a function of the fitting range for two different undercoolings and anisotropy strengths for simulations without melt flow. Here, R_{Iv} is the Ivantsov tip radius obtained from Eq. (1) using the tip velocity from the phase-field simulations [7]. The fitting range, measured as the distance behind the upstream tip, is specified as a multiple, n, of R_{Iv}. It can be seen from Fig. 7 that the ratio R_p/R_{Iv} indeed approaches unity with increasing fitting range. However, as shown by Karma et al. [7], a fitting range of about $10R_{Iv}$ is needed to obtain good agreement with the Ivantsov solution. Due to computer limitations, the results in Fig. 6 are only for a fitting range of up to $n = 3$. Fig. 7 shows that, for such a limited fitting range, the ratio R_p/R_{Iv} is equal to about 0.9. Hence, this explains the difference of up to 10% between the computed and theoretical growth Péclet numbers in Fig. 6. If a larger fitting range had been used for the simulations in Fig. 6, much better agreement in the growth Péclet numbers could be expected, even in the cases with flow. This was not possible because computer limitations prevented the use of a larger simulation domain and longer simulation times for the cases with flow. Also included in Fig. 7 is the ratio $R_{p\,max}/R_{Iv}$ as a function of the fitting range, where $R_{p\,max}$ is a tip radius obtained by fitting a parabola to the maximum ridge of the dendrite (see Fig. 4 and Section 4.5). For the relatively high anisotropy strengths used in the present simulations (0.04 and 0.05), the ratio $R_{p\,max}/R_{Iv}$ can be seen to continually increase with the fitting range, and it does not approach unity. This illustrates the importance of using the ECSA method [7] for evaluating the parabolic tip radius when comparing three-dimensional simulation results to the Ivantsov-type theories.

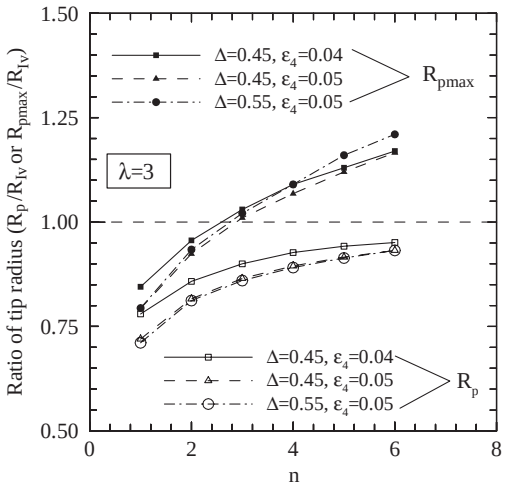

Fig. 7. Variation of the computed parabolic tip radius, R_p, using the ECSA method [7], and the maximum ridge parabolic tip radius $R_{p\,max}$, both normalized by the Ivantsov tip radius, R_{Iv}, as a function of the fitting range behind the tip, measured as a multiple, n, of R_{Iv}, for three different simulations without melt flow.

In summary, the relatively large (up to 10%) but systematic disagreement between the computed and theoretical growth Péclet numbers in Fig. 6 can be explained directly by an insufficient fitting range for evaluating the parabolic tip radius. The fact that the computed Pe_p for the two anisotropy strengths coincide well at a given flow Péclet

number indicates that other numerical inaccuracies do not play a major role in this comparison. Since the two theories do not differ by more than a few percent, it can be concluded that, if it had been possible to use a larger fitting range, the same kind of excellent agreement between computed and theoretical Pe_p as observed by Karma et al. [7] without flow can be expected with flow.

4.4. Operating state

The linear solvability analysis by Bouissou and Pelce [21], which assumes a two-dimensional parabolic cylinder dendrite tip shape, reveals that the ratio of the selection parameters without flow and with flow is a function of a dimensionless flow parameter χ

$$\chi = \frac{a(Re) d_0 U}{(15\varepsilon_e)^{3/4} R_p V}, \tag{13}$$

where $Re = UR_p/\nu = 2Pe_f/Pr$ is a flow Reynolds number, and $a(Re)$ is given in the two-dimensional case by

$$a_{2D}(Re) = \left(\frac{Re}{2\pi}\right)^{1/2} \frac{\exp(-Re/2)}{\mathrm{erfc}(\sqrt{Re/2})}. \tag{14}$$

For $\chi > \chi_c$, where χ_c is a critical threshold value much larger than unity, the following asymptotic form holds:

$$(\sigma_p^*)_0/\sigma_p^* = 1 + b\chi^{11/14}, \tag{15}$$

where $(\sigma_p^*)_0$ is the selection parameter without flow and b is a constant. For χ smaller than unity, which is the case in the present simulations, the ratio of selection parameters is independent of the flow parameter, i.e.

$$(\sigma_p^*)_0/\sigma_p^* \cong 1. \tag{16}$$

Physically, the analysis of Bouissou and Pelce [21] implies that flow has an effect on the tip selection parameter only if $(d_0 U)/(R_p V) = Pe_f \sigma_p^*$ is of the order of unity or greater.

For comparison with the present three-dimensional phase-field simulations, the above theory needs to be modified to be valid for a paraboloid of revolution, rather than for a two-dimensional parabolic cylinder as in Ref. [21]. An analysis performed within the course of the present study revealed that the only modification necessary is to replace the function in Eq. (14) by

$$a_{3D}(Re) = \frac{\exp(-Re/2)}{E_1(Re/2)}, \tag{17}$$

where E_1 is the exponential integral function.

Fig. 8 shows that, for the five simulations performed, the ratio $(\sigma_p^*)_0/\sigma_p^*$ of selection parameters without and with flow is nearly independent of the flow parameter, χ. Since $\chi < 0.4$ for all simulations, the phase-field results in Fig. 8 are in agreement with the linear solvability theory prediction, i.e. Eq. (16). The differences of up to 10% from the prediction can be attributed to inaccuracies in determining the parabolic tip radius from the phase-field results, as discussed in Section 4.3. In order to test the theory of Bouissou and Pelce [21] for $\chi \gg 1$ when Eq. (15) holds, simulations with much larger flow velocities and lower undercoolings need to be performed. Such simulations are presently outside the reach of available computer resources.

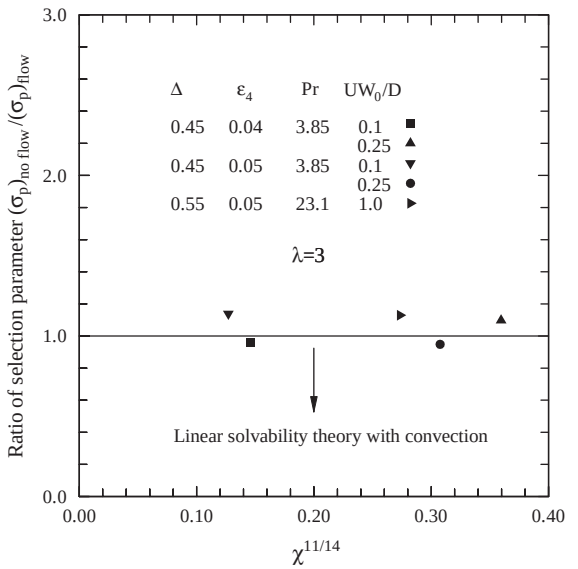

Fig. 8. Variation of the ratio of parabolic selection parameters without flow and with flow as a function of the dimensionless flow parameter, χ.

4.5. Three-dimensional tip morphology

It is of fundamental interest to investigate whether the universal non-axisymmetric dendrite tip shape relation by Ben Amar and Brener [4], Eq. (3), which was originally derived for purely diffusive heat transport, is still valid in the presence of melt convection. For this purpose, the computed upstream dendrite tip shapes are analyzed in this section for the following three simulation cases: the flow velocity, UW_0/D, is varied from 0, 0.1, to 0.25, while $\Delta = 0.45$, $\varepsilon_4 = 0.04$, $Pr = 3.85$, and $\lambda = 3$ are kept constant.

Fig. 9 shows longitudinal sections of the computed dendrite shape in the $\phi = 0^\circ$ plane (maximum ridge or fin) superimposed for $UW_0/D = 0$, 0.1, and 0.25. In this figure, the length coordinates, x and y, are measured from the upstream tip and are scaled by the parabolic tip radius, R_p, for each simulation case, as in Eq. (3). It can be seen that the three computed maximum ridge shapes coincide well. This indicates that the parabolic tip radius is still an appropriate scaling parameter for the dendrite tip shape in the presence of convection. The small differences in the contours for $x > 3$ between the no-flow and flow cases can be attributed to inaccuracies in determining R_p (see above).

Following the procedure of Karma et al. [7], the value of A_4 in Eq. (3) is obtained by minimizing the spatially averaged root-mean-square deviation between the computed maximum ridge shape and the fourth-order polynomial $x = y^2/2 - A_4 y^4$ over the interval $1 \leqslant x \leqslant n$, where n is a multiple of R_p. Note that for $\phi = 0^\circ$, $r = y$ and Eq. (3) becomes $x = y^2/2 - A_4 y^4$. Fig. 10 shows the variation of A_4 with n, obtained in this manner, for each of the three simulation cases. For purely diffusive heat transport, Karma et al. [7] found A_4 to be in the 0.004–0.005 range for $4 \leqslant n \leqslant 10$ (and much lower undercoolings and anisotropy strengths). The results for $UW_0/D = 0$ in Fig. 10 for $n \geqslant 4$ support this finding. The A_4 values for $n \leqslant 3$ can be disregarded due to an insufficient fitting range. The A_4 values obtained in the two flow cases appear to approach the same range as in the no-flow case. For $n = 4$, the A_4 values for all three simulations with and without flow are within a few percent of each other. Due to computer limitations, it was not possible in the two flow cases to obtain A_4 for a larger fitting range. Nonetheless, the present results indicate that, within the range

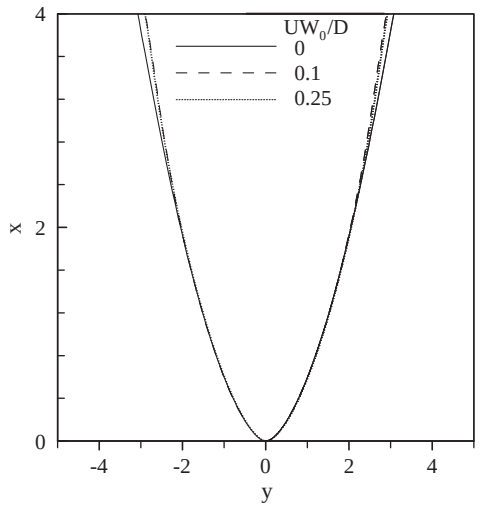

Fig. 9. Superposition of computed longitudinal upstream dendrite tip sections in the $\phi = 0^\circ$ plane (maximum ridge) for different flow velocities; all lengths are scaled by the parabolic tip radius, R_p ($\Delta = 0.45$, $\varepsilon_4 = 0.04$, $Pr = 3.85$, and $\lambda = 3$).

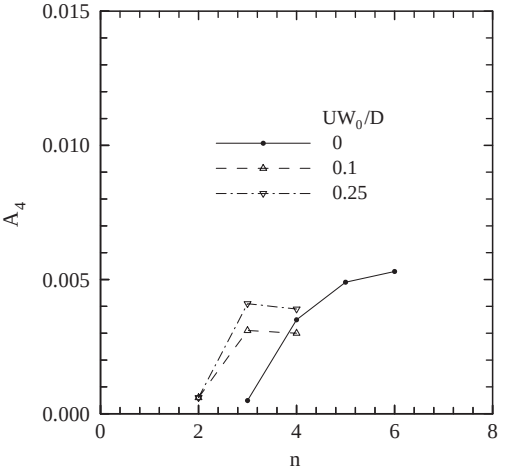

Fig. 10. Variation of A_4 with the fitting range, n, for different flow velocities; A_4 is obtained from a fit of the computed maximum ridge shape to the fourth-order polynomial representing the universal dendrite tip shape relation [4], Eq. (3), over the interval $1 \leqslant x \leqslant n$ ($\Delta = 0.45$, $\varepsilon_4 = 0.04$, $Pr = 3.85$, and $\lambda = 3$).

of flow velocities investigated, the universal value of A_4 remains unchanged in the presence of convection.

Fig. 11 examines the effect of convection on the entire non-axisymmetric tip shape. Transverse sections of the computed dendrite shape at $x = 2$ and 3 are superimposed in Figs. 11a and b, respectively, for all three simulation cases with and without flow. As in Fig. 9, all length coordinates are measured from the dendrite tip and are scaled by the parabolic tip radius, R_p, for each simulation case. It can be seen that the transverse sections in Fig. 11 are in nearly perfect agreement. This indicates that the scaled dendrite tip shape is the same with and without convection. In the purely diffusive regime, Karma et al. [7] already showed that the phase-field tip shape scales with the parabolic tip radius and is well described by the universal dendrite tip shape relation, Eq. (3), aside from a localized shape distortion near the tip, for a large range of anisotropy strengths and undercoolings. Even though phase-field results for only one anisotropy strength and undercooling are presented in this section, it appears from Figs. 9–11 that the same is true in the presence of convection. Clearly, a larger range of flow velocities and Prandtl numbers should be investigated in the future.

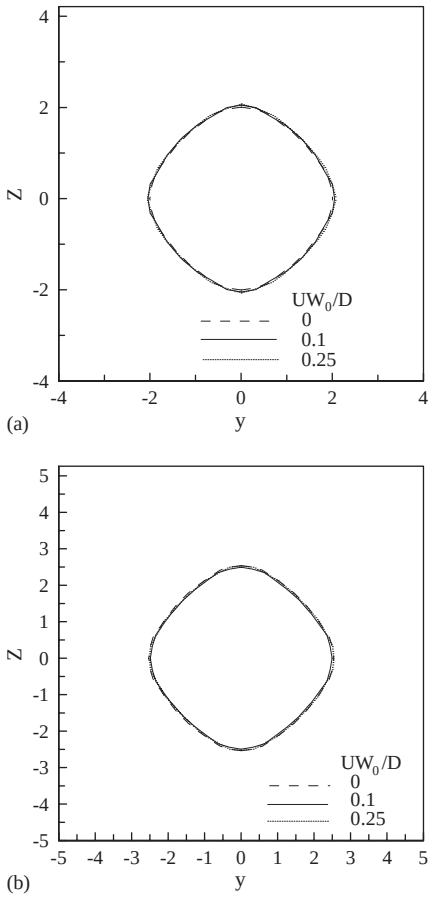

Fig. 11. Superposition of computed transverse upstream dendrite tip sections at (a) $n = 2$ and (b) $n = 3$ for different flow velocities; all lengths are scaled by the parabolic tip radius, R_p ($\Delta = 0.45$, $\varepsilon_4 = 0.04$, $Pr = 3.85$, and $\lambda = 3$).

5. Conclusions

Free dendritic growth of a pure material into an undercooled melt in the presence of fluid flow is investigated in three dimensions using the phase-field method. The Navier–Stokes equations for the flow and the energy equation for the heat transport are solved numerically on a grid that is twice as coarse as the grid for the phase-field equation. The effect of the flow on the dendritic growth is investigated as a function of the imposed flow velocity, undercooling, anisotropy strength, and Prandtl number. The results for the upstream tip are compared to available theories of dendritic growth. The predicted growth Péclet numbers as a function of the flow Péclet number are in good agreement with the theoretical predictions when taking into account that the fitting range for evaluating the parabolic dendrite tip radius was somewhat insufficient. The dendrite tip selection parameter is essentially independent of the flow velocity within the range studied, which is also in accordance with theory. The three-dimensional dendrite tip shape in the presence of convection is found to be well fitted by the same universal scaling relation as without flow. Future work should concentrate on performing simulations for larger domain sizes, in order to allow for increased fitting ranges. In addition, larger ranges of the governing dimensionless parameters should be investigated. Simulations with higher flow velocities would be of particular interest in order to

test the linear solvability theory relation for the tip selection parameter in the regime where it is predicted to significantly change from the no-flow value. Much lower Prandtl numbers simulations could help in clarifying the effect of convection on dendritic growth in metallic systems.

Acknowledgements

This work was supported by NASA under Contracts NCC8-094 and NNM04AA18G. The authors thank Prof. Turek of the University of Dortmund, Germany, for his help with the FEATFLOW code, and Prof. A. Karma of Northeastern University, Boston, MA, for making the three-dimensional phase-field code (without flow) available to us.

References

[1] G.P. Ivantsov, Dokl. Akad. Nauk SSSR 58 (1947) 567.
[2] J.S. Langer, in: J. Souletie, J. Vannimenus, R. Stora (Eds.), Chance and Matter, Lectures on the Theory of Pattern Formation, Les Houches, Session XLVI, North-Holland, Amsterdam, 1987, pp. 629–711.
[3] D. Kessler, J. Koplik, H. Levine, Adv. Phys. 37 (1988) 255.
[4] M. Ben Amar, E. Brener, Phys. Rev. Lett. 71 (1993) 589.
[5] E. Brener, V.I. Melnikov, JETP 80 (1995) 341.
[6] A. Karma, W.-J. Rappel, Phys. Rev. Lett. 77 (1996) 4050; A. Karma, W.-J. Rappel, Phys. Rev. E 57 (1988) 4323.
[7] A. Karma, Y.H. Lee, M. Plapp, Phys. Rev. E 61 (2000) 3996.
[8] M.E. Glicksman, M.B. Koss, E.A. Winsa, Phys. Rev. Lett. 73 (1993) 573.
[9] J.C. LaCombe, M.B. Koss, V.E. Fradkov, M.E. Glicksman, Phys. Rev. E 52 (1995) 2778.
[10] U. Bisang, J.H. Bilgram, Phys. Rev. Lett. 21 (1995) 3898; U. Bisang, J.H. Bilgram, Phys. Rev. E 54 (1996) 5309.
[11] S.C. Huang, M.E. Glicksman, Acta Metall. 29 (1981) 701.
[12] Y.W. Lee, R.N. Smith, M.E. Glicksman, M.B. Koss, Ann. Rev. Heat Transfer 7 (1996) 59.
[13] S.K. Dash, W.N. Gill, Int. J. Heat Mass Transfer 27 (1984) 1345.
[14] R. Ananth, W.N. Gill, Chem. Eng. Commun. 68 (1988) 1.
[15] R. Ananth, W.N. Gill, J. Crystal Growth 91 (1988) 587.
[16] R. Ananth, W.N. Gill, J. Crystal Growth 108 (1991) 173.
[17] D.A. Saville, P.J. Beaghton, Phys. Rev. A 37 (1988) 3423.
[18] M. Ben Amar, Ph. Bouissou, P. Pelce, J. Crystal Growth 92 (1988) 97.
[19] J.-J. Xu, J. Fluid Mech. 263 (1994) 227.
[20] Y.W. Lee, W.N. Gill, R. Ananth, Chem. Eng. Commun. 116 (1992) 193.
[21] Ph. Bouissou, P. Pelce, Phys. Rev. A 40 (1989) 6673.
[22] Ph. Bouissou, B. Perrin, P. Tabeling, Phys. Rev. A 40 (1989) 509.
[23] V. Emsellem, P. Tabeling, J. Crystal Growth 156 (1995) 285.
[24] Y.W. Lee, R. Ananth, W.N. Gill, J. Crystal Growth 132 (1993) 226.
[25] R. Ananth, W.N. Gill, J. Crystal Growth 179 (1997) 263.
[26] H.J. Diepers, C. Beckermann, I. Steinbach, in: J. Beech, H. Jones (Eds.), Solidification Processing 1997, Ranmoor House, Sheffield, 1997, pp. 426–430.
[27] C. Beckermann, H.J. Diepers, I. Steinbach, A. Karma, X. Tong, J. Comput. Phys. 154 (1999) 468.
[28] R. Tönhardt, G. Amberg, J. Crystal Growth 194 (1998) 406.
[29] D.M. Anderson, G.B. McFadden, A.A. Wheeler, Physica D 135 (2000) 175.
[30] X. Tong, C. Beckermann, A. Karma, Phys. Rev. E 61 (2000) R49.
[31] R. Tönhardt, G. Amberg, Phys. Rev. E 62 (2000) 828.
[32] R. Tönhardt, G. Amberg, J. Crystal Growth 213 (2000) 161.
[33] X. Tong, C. Beckermann, A. Karma, Q. Li, Phys. Rev. E 63 (2001) 061601.
[34] C.W. Lan, C.M. Hsu, C.C. Liu, J. Crystal Growth 241 (2002) 379.
[35] C.W. Lan, C.M. Hsu, C.C. Liu, Y.C. Chang, Phys. Rev. E 65 (2002) 061601.
[36] E. Bansch, A. Schmidt, Interfacial Free Boundaries 2 (2000) 313.
[37] S.W. Shin, D. Juric, J. Mech. Behav. Mater. 11 (2000) 313.
[38] H.S. Udaykumar, R. Mittal, P. Rampunggon, A. Khanna, J. Comput. Phys. 174 (2001) 345.
[39] N. Al-Rawahi, G. Tryggvason, J. Comput. Phys. 180 (2002) 471.
[40] J.-H. Jeong, N. Goldenfeld, J.A. Dantzig, Phys. Rev. E 64 (2001) 041602.
[41] J.-H. Jeong, J.A. Dantzig, N. Goldenfeld, Metall. Mater. Trans. A 34 (2003) 459.
[42] Y. Lu, C. Beckermann, A. Karma, in: Materials Researh Society Symposium Proceedings, vol. 701, MRS, Warrendale, PA, 2002, pp. T2.2.1–T2.2.10
Y. Lu, C. Beckermann, A. Karma, in: Proceedings of ASME IMECE 2002, ASME, New York, NY, 2002, Paper No. IMECE2002-32838.
[43] N. Al-Rawahi, G. Tryggvason, J. Comput. Phys. 194 (2004) 677.
[44] A. Karma, W.-J. Rappel, Phys. Rev. E 53 (1996) R3017.
[45] S. Turek, Int. J. Numer. Methods Fluids 18 (1994) 71.
[46] FEATFLOW, http://www.featflow.de.
[47] Y. Lu, Ph.D. Dissertation, The University of Iowa, Iowa City, IA, 2003, pp. 77–97.
[48] D.J. Tritton, J. Fluid Mech. 6 (1959) 547.
[49] B. Huner, R.G. Hussey, Phys. Fluids 20 (1977) 1211.
[50] J.-H. Jeong, J.A. Dantzig, N. Goldenfeld, Personal Communication, Iowa City, IA, 2002.